

# On a turbulent wall jet flowing over a circular cylinder

By R. NEUENDORF AND I. WYGNANSKI

AME Department, University of Arizona, Tucson, AZ 85721, USA

(Received 30 April 1997 and in revised form 19 June 1998)

The effect of surface curvature on the development of a two-dimensional wall jet was investigated experimentally. A comparison was made between a wall jet flowing around a circular cylinder and its plane equivalent. Velocity surveys and surface pressure measurements in the curved wall jet suggest the existence of two primary regions of interest. The first region, ranging from the end of the potential core to an approximate angular position of  $\theta = 120^\circ$ , is characterized by a constant surface pressure and a self similarity of the mean flow. The second region is marked by an adverse pressure gradient leading to separation around  $\theta = 230^\circ$ . The rate of spread of this flow, even in the initial region, is much higher than in the plane wall jet and so are the levels of turbulence and Reynolds stress. The dominant lengthscale in this flow is the radius of curvature  $R$  and the dominant velocity scale is the square root of the kinematic jet momentum divided by the radius of curvature. Entrainment of ambient fluid which causes the jet to adhere to the curved surface is also the main reason for its separation which is preceded by a rapid rate of spread of the flow leading to the failure of the boundary-layer approximation.

---

## 1. Introduction

Wall jets are used to delay boundary-layer separation, to provide supercirculation on lifting surfaces and to either enhance or suppress convective heat transfer between a surface and the fluid surrounding it. Probably the most familiar application of a wall jet is to defrost or demist car windshields; however, its use in cooling turbine blades or preventing separation over slotted flaps is no less important. In many applications a jet flows over a curved surface such as a turbine blade or flap. In some instances curvature is used to generate supercirculation by altering the position of the rear stagnation point (i.e. the location at which the flow separates from the surface). Recently, a wall jet flowing over a circular cylinder has replaced the tail rotor used to prevent the autorotation of a typical helicopter. The NOTAR, as it is called (NO Tail Rotor), may make a helicopter lighter, safer and quieter.

Some shortcomings in the understanding of the wall jet flowing over a circular cylinder became apparent during the development of the NOTAR. Early versions required that fences (similar to boundary-layer fences used on swept-back wings) be mounted to its boom. These fences generated a large drag force in forward flight and were later replaced by two blowing slots whose relative location was determined empirically. This design revision would not have been necessary if the detailed structure of this important flow had been thoroughly understood.

The purpose of the present investigation is to determine the effects of streamline curvature on this flow and to assess the causes leading to its separation from the

surface. The attachment of a jet to an adjacent curved surface was discussed some two hundred years ago by Young (1800) and patented a century later by Coanda. It is therefore, widely referred to as the ‘Coanda effect’. Although Rayleigh (1916) determined the conditions for stability of the curved flow, the effect of streamwise curvature on the evolution of the wall jet was mostly ignored until 1961 when Newman published his seminal paper. This was followed by the publications of Fekete (1963), Guitton (1964), Wilson & Goldstein (1976), Fujisawa & Kobayashi (1987), and others. It was recognized that streamwise curvature generates an instability in the outer part of the wall jet affecting the turbulence generation and its transport across the flow. It was also acknowledged that turbulent equilibrium is unattainable over a circular cylinder in spite of the apparent self similarity of the mean motion which extends over most of the attached-flow region. Many of the above mentioned investigations focused on the comparison between the flow over a plane surface and over a circular cylinder and attempted to accomplish it on a single experimental facility. For this reason the jet emerged from a settling chamber exterior to the cylinder (e.g. Fujisawa & Kobayashi), in most applied systems (e.g. NOTAR or film cooling), however, the jet emerges from within the cylinder. It was noted that the external settling chamber sets up an adverse pressure gradient initiating a premature separation of the flow from the surface. Thus, only an internal settling chamber should be used in an experiment to study the contribution of streamwise curvature to flow separation. The experimental facility designed by Newman and Fekete provides such an opportunity. The present data is compared to measurements made on a plane wall jet by Zhou, Heine and Wygnanski (1996).

The tests were carried out on a smooth, circular cylinder at slot Reynolds numbers ranging from  $3 \times 10^3$  to  $13 \times 10^3$ . Taps drilled through the cylinder walls were used to provide mean surface pressure data, while velocity measurements were carried out using hot-wire anemometers.

## **2. Apparatus and data acquisition**

The experiments were carried out on a highly polished, (radius  $R = 101.6$  mm circular cylinder, made out of a thick aluminium pipe 914.4 mm long that is spliced along its entire length to provide a nozzle, as shown in figure 1. The interior space of the cylinder contains the settling chamber, screens, and a contraction through which the jet emerges tangentially to the exterior surface. The width of the nozzle,  $b$ , which spans the entire cylinder, can be altered by the addition of spacers at the foot of the upper lip. The initial aspect ratio of the jet varied, therefore, between 130 and 390, depending on the spacers used. The cylinder was mounted on bearings embedded inside two large end-plates that allowed rotation around its axis.

The airflow was provided by a centrifugal blower that was powered by a frequency-controlled a.c. motor. It entered the settling chamber through both ends of the cylinder. Before entering the blower, the air passed through a temperature controlled chamber equipped with cooling coils and a heater that equated the temperature of the jet to the ambient air at all speeds considered. The maximum temperature differential between the two flows did not exceed  $\pm 0.5^\circ\text{C}$ .

The hot-wire probe was mounted on a single-axis traverse system in a direction perpendicular to the surface. A computer-controlled stepper motor was used to achieve a resolution of  $\frac{1}{630}$  mm per step. The circumferential distance between the probe and the nozzle was altered by rotating the cylinder. Movements in the spanwise direction were accomplished by sliding the traverse on a rail attached to the end-plates

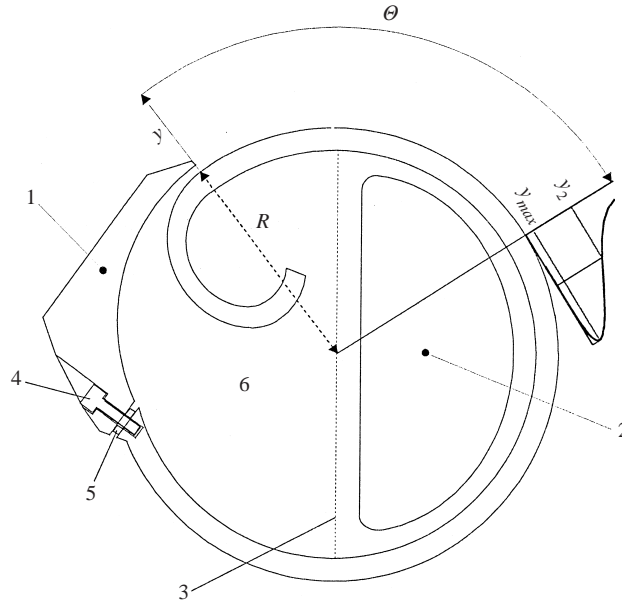


FIGURE 1. Cross-section of the apparatus. 1. Upper lip. 2. Air supply. 3. Screens. 4. Tightening screw. 5. Spacer. 6. Plenum chamber.

and located well above the surface of the cylinder. This freedom of movement was necessary to verify the two-dimensionality of the flow.

The momentum emanating from the nozzle was actually measured by integrating the velocity profile at the slot exit (figure 2), not relying on the assumption that the flow at the slot has a 'top hat' velocity profile. The calibration yielded:

$$0.89 < 2\rho \int_0^{\infty} \overline{u^2} dy / (p_0 - p_{\infty}) b \leq 0.93,$$

and the results were normalized by the measured jet momentum. Since the hot wires were calibrated in a separate calibration jet, one could show that the pressure difference between the settling chamber and the room was less than the dynamic pressure [i.e.  $(p_0 - p_{\infty}) < \frac{1}{2}\rho U_{jet}^2$ ], suggesting that the flow expands to some local static pressure,  $p_s$ , that is lower than atmospheric. However, since all pressure distributions reported in the literature are normalized by  $(p_0 - p_{\infty})$  and in view of the losses resulting from the boundary layers (figure 2) which more than offset the gains calculated by using  $(p_0 - p_s)$  the correction to the kinematic jet momentum,  $J$ , was neglected.

The two-dimensionality of the flow was tested at a few distances from the nozzle. Close to the nozzle exit, the variations in the maximum velocity did not exceed 0.2% of the average value over most of the span (i.e. for spanwise distances ranging from  $-2 < z/R < 3$ ).

Cross-wires were calibrated at numerous velocities (up to the maximum velocity anticipated in the specific test) and yaw angles. The calibration range in yaw was  $\pm 42^\circ$ . Look-up tables that were created during the calibration procedure were not only used to convert voltages to velocities but also to check that calibration limits were not exceeded. Whenever the output voltage of a given wire exceeded its calibration limit, the event was noted and the total times of such excesses were recorded. This information provides a good estimate of the accuracy of the data. The instantaneous

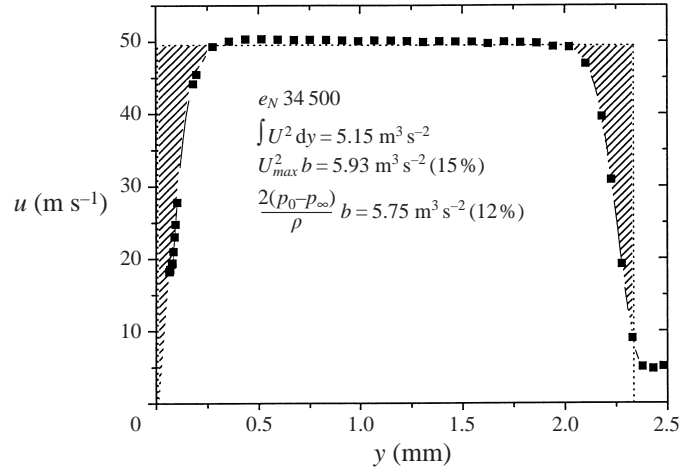
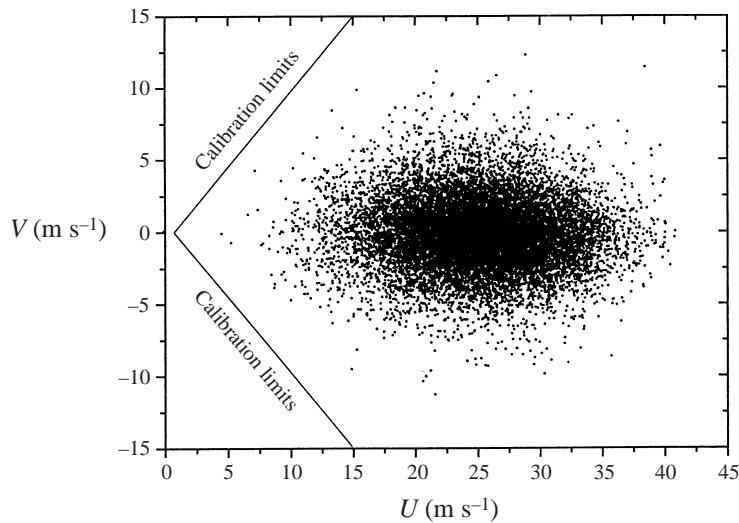


FIGURE 2. Mean velocity profile at the nozzle.

FIGURE 3. Set of instantaneous velocity pairs ( $U, V$ ) from a hot-wire signal mapped into the  $\times$ -wire calibration domain.

voltage outputs of a pair of wires (in an  $\times$ -array) located in the flow are plotted in figure 3 as an example. The calibration limits of the  $\times$ -array are also shown on this figure. The percentage difference between the total measurement time and the time spent outside the calibration limits is referred to as the validation ratio  $r_{valid}$ .

Since doubts were cast on the validity of data acquired with a hot wire, some results were compared to data acquired by a laser-Doppler anemometer (LDA). The profiles of the streamwise component of velocity and turbulent intensity measured at three azimuthal locations  $60^\circ$ ,  $140^\circ$  and  $180^\circ$  are plotted in figure 4. The single wire results are shown by solid curves whereas symbols describe LDA data. The validation ratio  $r_{valid}$  that was used for the  $\times$ -array is also shown on these figures near the right ordinate.

The agreement between the two sets of data is very good over most of the

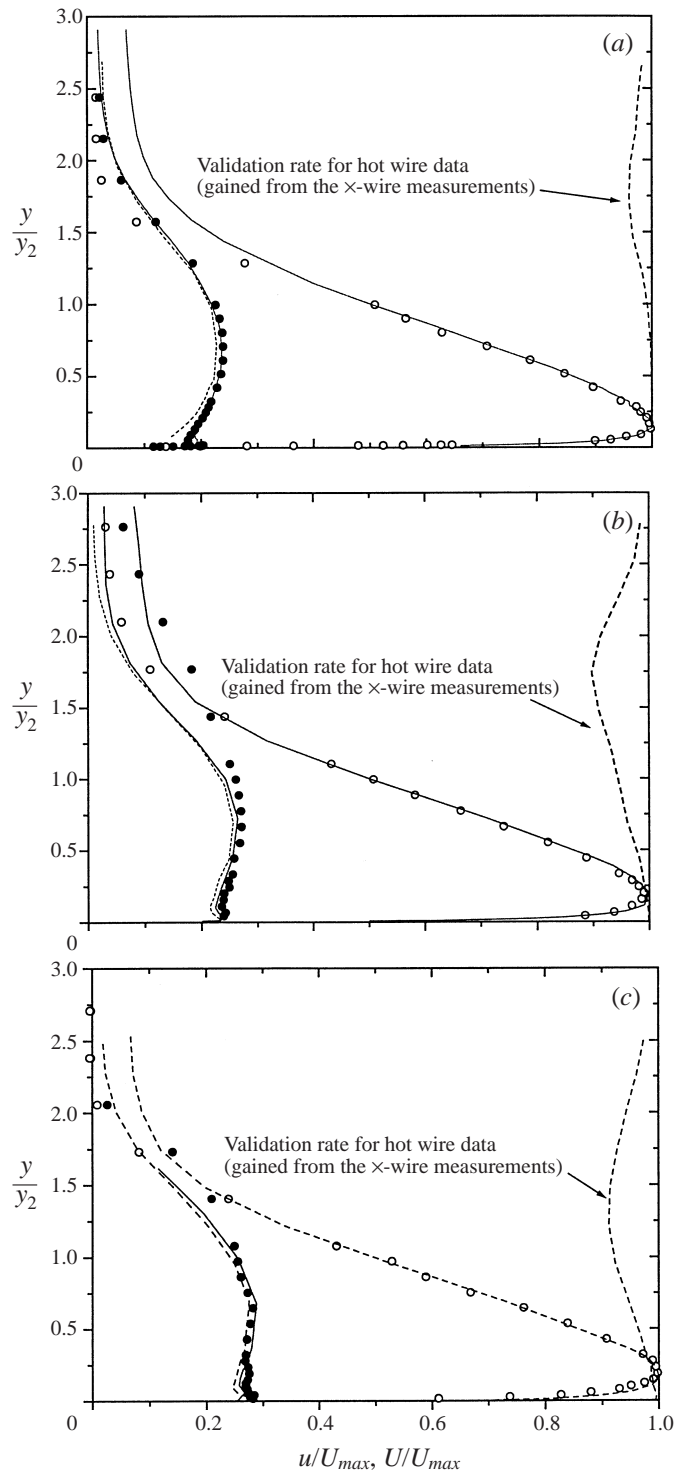


FIGURE 4. A comparison of hot wire and LDV measurements at three azimuthal locations (a)  $60^\circ$ , (b)  $140^\circ$ , (c)  $180^\circ$ , ●, ○, LDA; —, single hot wire; ---, × hot wire.

measurement domain. The mean velocities measured by a single wire in the outer region ( $y/y_2 > 1.5$ ) are generally higher than those measured by the LDA partly because of the lack of sensitivity of the wire to the flow direction and partly because of the high turbulence intensity in this region. Velocities measured with an  $X$ -array differed very slightly from the measurements made with a single wire in this region. It appears that mean velocities measured by hot wires are reliable whenever the validation ratio exceeds 95% and where the local turbulent intensity is less than 50%.

Wherever the flow was separated even intermittently (i.e. at  $\theta > 200^\circ$ ) the insensitivity of the hot wire to directional changes resulted in  $r_{valid} < 90\%$ , and it increased the discrepancy between measurements made with an LDA and a hot wire. Intermittent separation affected mostly the measurements of turbulence intensity and not mean velocity, as the high turbulence intensity did in the outer part of the wall jet. Because of this uncertainty the results presented and discussed below focus on the region bound by  $40^\circ < \theta < 200^\circ$ . The skin friction estimation was made from the slope of the mean velocity profile in the immediate vicinity of the wall. Great care, therefore, was exercised to measure  $(dU/dy)$  as precisely as possible. A comparison between LDA and hot-wire data measured in the immediate vicinity of the surface is shown in figure 5 for  $\theta = 60^\circ$  and for  $120^\circ$ . The comparison between the two sets of results is excellent and would result in identical skin friction coefficient. Consequently, the various momentum budgets presented below are accurate and reaffirm the two-dimensionality of the mean flow.

Measurements done with an LDA (and a particle image velocimeter) proved to be sensitive to the source of the seeding, particularly at small values of  $\theta$ . Smoke introduced into the settling chamber biased the mass flow emanating from the nozzle, whereas smoke introduced to the ambient fluid accentuated the entrained flow. Thus, the radial velocities measured by tracking the particles could have had an opposite sign, depending on their origin.

### 3. The mean velocity profiles

Mean velocity profiles were measured for several jet exit velocities and slot widths, but only a sample of the data is presented for the sake of clarity. All of the data discussed initially correspond to a single slot width of 2.34 mm and an exit velocity of  $U_{jet} = 48 \text{ m s}^{-1}$  (see figure 6), and thus a nominal Reynolds number  $Re_N \equiv \left(\frac{1}{2}U_{jet}^2 bR/\nu^2\right)^{1/2} = 33\,000$  (the reason for the choice of this lengthscale will be apparent later).

A fully developed velocity profile typical of the wall jet flow was observed for this case at an angular position  $\theta \approx 20^\circ$ . At much larger slot widths the potential core might not have terminated at this location and thus, the first mean velocity profile presented in figure 6 was taken at  $\theta = 40^\circ$ . Since the surface pressure is almost constant up to  $\theta = 120^\circ$ , an attempt was made to plot all the velocity profiles in self-similar coordinates in order to assess the effect of constant curvature on the development of this flow (figure 6). The mean velocity distribution in the curved wall jet is almost indistinguishable from the plane wall jet when it is normalized by the local maximum velocity  $U_{max}$  and the distance from the wall  $y_2$  at which the velocity in the outer part of the flow is equal to  $\frac{1}{2}U_{max}$ . The variation of the local length and velocity scales with distance from the nozzle will be examined later. The average location of the maximum velocity occurred at  $y/y_2 = 0.16$ , which agrees with the corresponding value for the plane wall jet (Wygnanski, Katz & Horev 1992). The absence of a

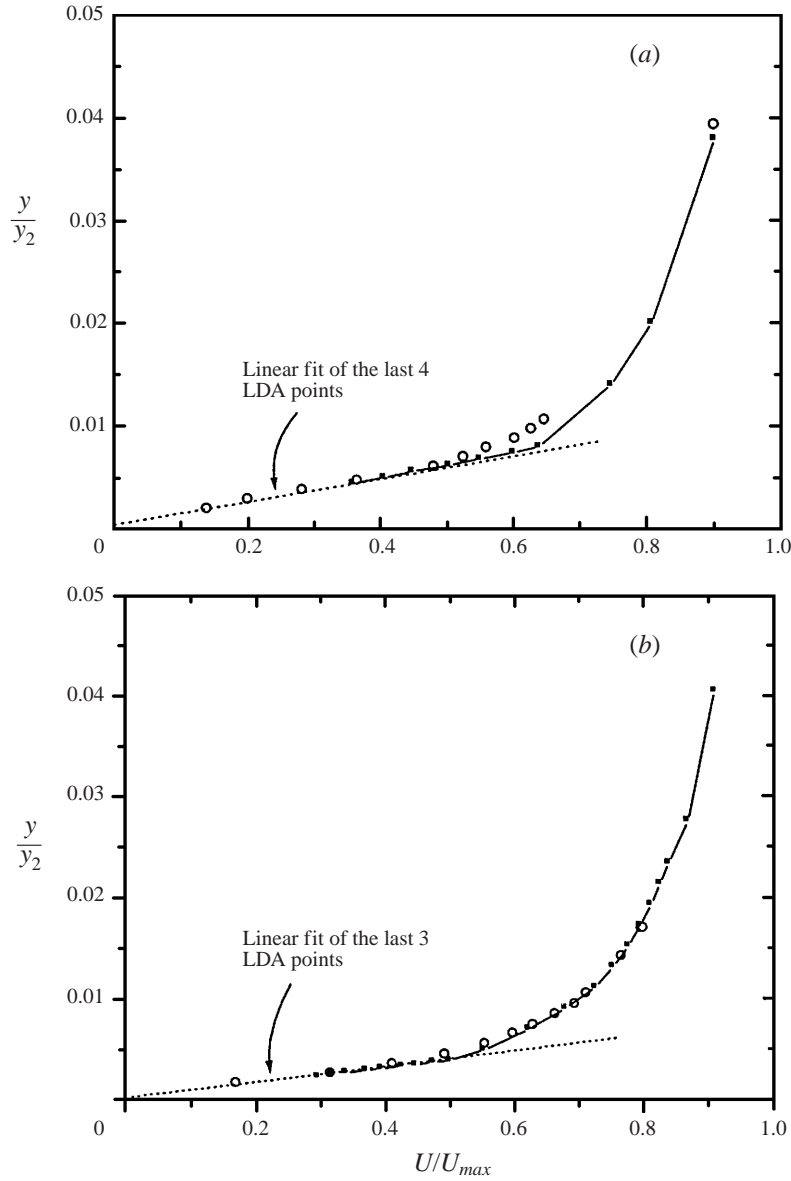


FIGURE 5. A comparison of hot-wire and LDV measurements near the surface at two azimuthal locations (a)  $60^\circ$ , (b)  $120^\circ$ .  $\circ$ , LDA;  $\blacksquare$ , single hot wire.

free stream contributes to the scatter in the data at large values of  $y/y_2$  where the direction of the flow is uncertain and the turbulence level is high. The curved wall jet appears to have a higher velocity gradient near the surface than the plane wall jet (figure 6b), but this is a consequence of the scaling and it does not suggest that the skin friction coefficient  $c_f$  is higher. The measurements near the surface agree with previous experiments by Fujisawa & Kobayashi and by Wilson & Goldstein (1976), although the last two authors do not even comment on the matter of skin friction. Supplementary investigation at  $60^\circ < \theta < 120^\circ$  indicated that the skin friction coefficient is actually reduced compared to the plane wall jet. This is consistent with the

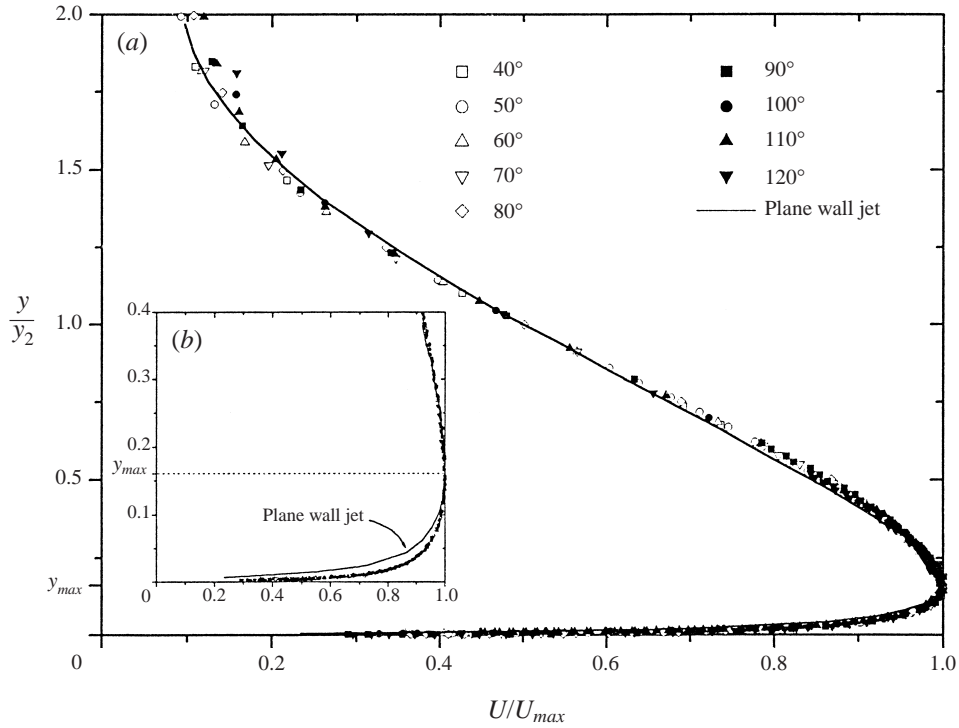


FIGURE 6. A comparison between mean velocity profiles in the constant pressure region and the plane wall jet. Scaled with the half width  $y_2$  and  $U_{max}$ .

observations made in a thin boundary layer evolving over a slightly convex surface (unpublished work by R. N. Merony referred to in Bradshaw 1969). It will become apparent that this flow lacks the necessary conditions for self preservation and it is not in a state of moving equilibrium as required by Townsend (1956).

As one moves farther downstream, into the adverse pressure gradient region, the similarity of the mean velocity profiles fails (figure 7a). Between  $140^\circ < \theta < 180^\circ$  the deviations are small and are mostly perceptible in the inner region when viewed on an expanded scale (figure 7b). Beyond  $\theta > 180^\circ$ , the thickness of the inner boundary layer increases rapidly with increasing  $\theta$ , moving the location of the maximum velocity  $y_{max}$  outward relative to the local width of the jet  $y_2$ . A new lengthscale ( $y_2 - y_{max}$ ) is required to maintain an approximate self similarity in the outer part (i.e.  $y - y_{max} > 0$ ) of the mean velocity profile; however, there is no obvious length capable of scaling the inner part of the flow (figure 7c).

The changes occurring in the mean velocity distribution of the inner region increase as the flow approaches the separation location. The adverse pressure gradient shown in figure 8 contributes to this lack of self similarity, as it often does in a turbulent boundary layer. For example, the shape factor  $H$ , ratio of local displacement thickness to local momentum thickness, of the inner boundary layer responds to the adverse pressure gradient by increasing from  $H = 1.3$  at  $\theta \approx 180^\circ$  to  $H = 2.1$  at  $\theta = 220^\circ$ . By extrapolating this curve (figure 8) to  $\theta = 240^\circ$  the value of  $H$  near separation would be very close to the accepted values for turbulent boundary layers.

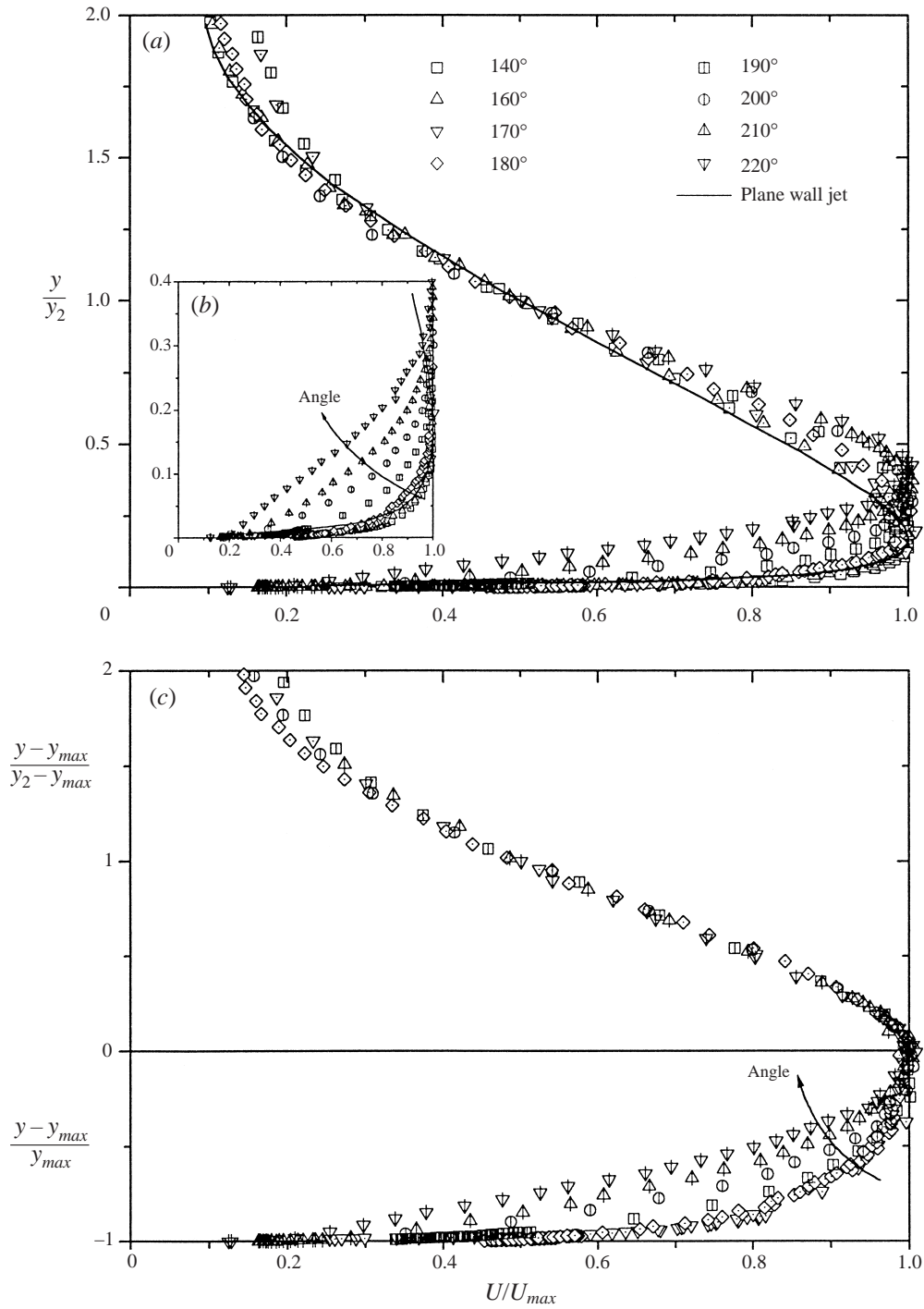
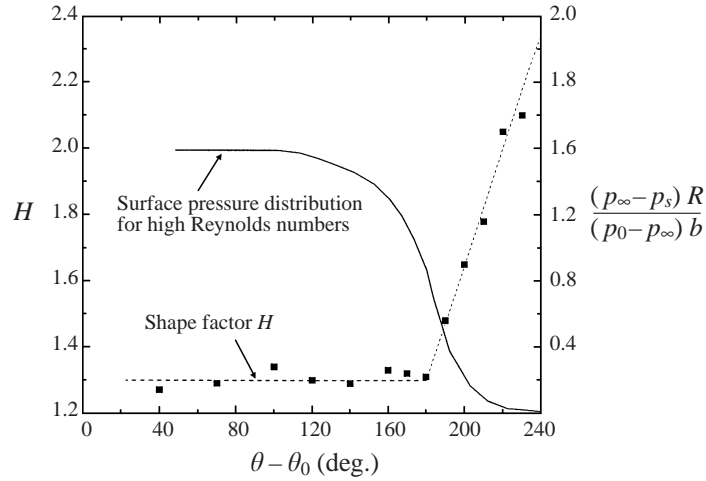


FIGURE 7. The mean velocity distribution in the adverse pressure region. (a), (b) Scaled with one lengthscale  $y_2$  and one velocity scale  $U_{max}$ . (c) Scaled with two lengthscales  $y_{max}$  and  $y_2 - y_{max}$  and one velocity scale  $U_{max}$ .

FIGURE 8. Inner boundary-layer shape factor  $H$  and surface pressure coefficient  $c_p$ .

#### 4. Length and velocity scales

The decay of the maximum velocity in the jet and its radial rate of spread in the direction of streaming are first plotted using the traditional scaling (e.g. Launder & Rodi 1981) in figure 9 and compared with corresponding data obtained for the plane wall jet. The arc length  $R\theta$  represents also the distance  $x$  because the boundary-layer coordinates follow the surface. This distance is measured from a virtual origin  $\theta_0$  obtained by extrapolating the data in the self similar region. Since the maximum velocities in plane wall jets decay approximately as  $U_{max} \propto x^{-1/2}$ , the ratio of  $(U_{jet}/U_{max})^2$  could have been expected to vary almost linearly with  $x$ , or rather with  $R\theta$ , as indicated by the solid lines obtained for the plane wall jet at corresponding  $Re_j = U_{jet}b/\nu$  (figure 9a). The maximum velocities in the curved wall jet decrease much faster with  $x$  than in the plane flow. This must be accompanied by an increased rate of spread (figure 9b), otherwise the momentum loss to skin friction would have been unreasonable. It is clear that traditional scaling using the slot width as the reference lengthscale does not collapse the data onto a single universal curve for different slot widths. Since the mean velocity profiles are self similar, provided  $\theta \leq 180^\circ$ , the local kinematic jet momentum can be obtained:

$$J = U_{max}^2 y_2 \underbrace{\int_{y/y_2=0}^{\infty} \left( \frac{U}{U_{max}} \right)^2 d \left( \frac{y}{y_2} \right)}_{const} = 0.78 U_{max}^2 y_2 \quad (1)$$

from the product of the length and velocity scales. The decay of  $J$  in the direction of streaming is very gradual. In the constant surface pressure region ( $40^\circ \leq \theta \leq 120^\circ$ ), the skin friction appears to have little or no influence on the evolution of the flow, although the presence of the solid surface affects the scale of the large eddies which are smaller than in a corresponding free jet.

It was recognized by Narasimha, Narayan & Parthasarathy (1973) and reinforced by Wygnanski *et al.* (1992) that the details of the flow through the nozzle cannot influence the overall behaviour of the turbulent wall jet far downstream of its origin. Thus the dimension of the nozzle becomes irrelevant. The flow in the absence of curvature scaled with the initial, kinematic momentum flux  $J$  and the fluid viscosity

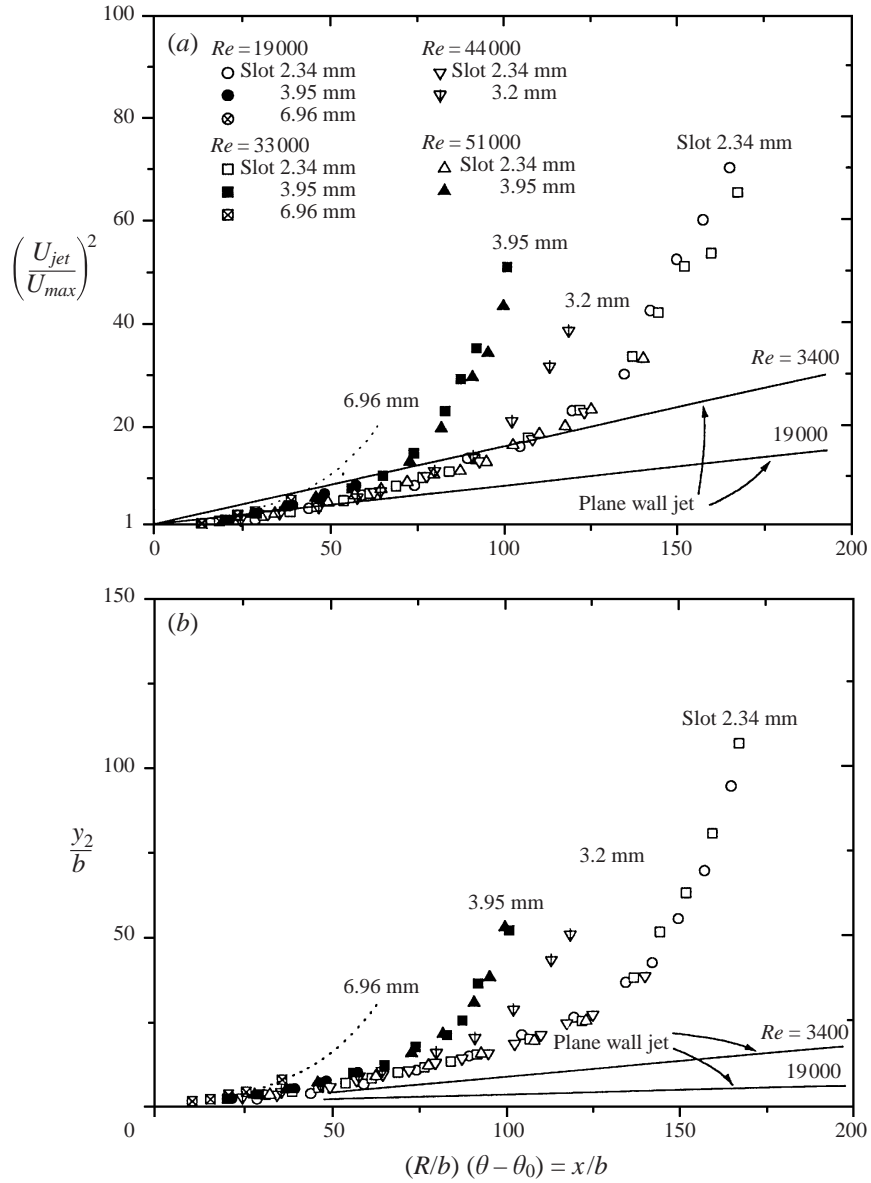


FIGURE 9. (a) The decay of the maximum velocity and (b) radial rate of spread in the direction of streaming. Scaling based on the jet exit velocity  $U_{jet}$  and the slot width  $b$ .

$\nu$ , rather than the slot width  $b$  and the exit velocity  $U_{jet}$ . The length and velocity scales derived from these two independent parameters are  $\nu^2/J$  and  $J/\nu$ , respectively. The practical demonstration that the flow is indeed independent of the conditions at the nozzle was provided by Zhou, Rothstein & Wygnanski (1992) who collapsed all the available mean flow data on wall jets onto universal curves independent of  $Re_j = U_{jet} b/\nu$ . It should be noted that the new length and velocity scales based on  $J$  and  $\nu$  define a Reynolds number which is equal to unity regardless of the conditions at the nozzle.

The evolution of an incompressible wall jet around the circular cylinder of radius

$R$ , depends on  $J$ ,  $\nu$  and on  $R$ . The significance of the additional lengthscale  $R$  is apparent when the ratio of  $y_2/R$  is no longer small. In this instance, the boundary-layer approximation may no longer apply, imposing a new limitation on the slot width (i.e.  $b/R \ll 1$ ). Assuming that the relevant length and velocity scales in the present flow are:  $R$  and  $(J/R)^{1/2}$ , respectively, then the relevant Reynolds number,

$$Re_N \equiv \frac{(J/R)^{1/2} R}{\nu} = \frac{(JR)^{1/2}}{\nu}, \quad (2)$$

instead of being a constant as it was in the plane wall jet. Thus, the relevance of the above mentioned  $Re_N$  is clearly demonstrated by plotting  $y_2/\nu^2 J$  and  $U_{max}/J/\nu$  versus the dimensionless distance from the nozzle  $R\theta/\nu^2/J$  (figure 10), since the data fall on separate curves characterized by  $Re_N$ . In the limit of a very thin wall jet or very large  $R$ , all curves collapse onto a line representing the plane flow. The ratio  $b/R$  is of no significance within the bounds of  $b/R$  considered here since each curve representing a constant  $Re$  contains three values of  $b/R < 0.07$ . These figure suggest that each dependent dimensionless variable in this flow is a function of two independent parameters:  $\theta$  and  $Re_N$  (see also Newman 1961).

The dimensionless local width of the flow,  $y_2/R$  and the concomitant maximum velocity  $U_{max}/(J/R)^{1/2}$  are plotted against the angular distance from the virtual origin for each case (i.e. for various  $Re$  and  $b/R$ ) and found to collapse onto a single curve, suggesting that the flow is independent of  $Re$  provided the latter is larger than  $19 \times 10^3$  (see figure 11). The data are well represented by

$$\left. \begin{aligned} \frac{y_2}{R} &= 0.11(\theta - \theta_0)^{1.46}, \\ \frac{U_{max}}{(J/R)^{1/2}} &= 3.35(\theta - \theta_0)^{-0.76}, \end{aligned} \right\} \quad (3)$$

in the constant pressure region corresponding to  $40^\circ \leq \theta - \theta_0 \leq 120^\circ$  and may in most instances be extrapolated to  $\theta - \theta_0 = 180^\circ$ . The results of Wilson & Goldstein are also plotted in figure 11 for comparison. The agreement between these two sets of data is good up to  $\theta - \theta_0 = 120^\circ$ , the deviations at larger distances from the nozzle are attributed to the exterior settling chamber used by these investigators. Equation (3) yields

$$\frac{y_2 U_{max}^2}{J} = 1.23(\theta - \theta_0)^{-0.06}, \quad (4)$$

and the self consistency of the similarity assumption comes out when one substitutes for  $J = 0.78 U_{max}^2 y_2$  from equation (1) to give

$$1.28 \approx 1.23(\theta - \theta_0)^{-0.06}. \quad (5)$$

## 5. Surface pressure

The pressure differential across the flow balances the centrifugal force generated by the wall jet as it follows the circular path along the surface of the cylinder. Boundary-layer equations may describe the flow adequately provided  $y_2/R \ll 1$ . The mean momentum equation in the direction normal to the streamlines is:

$$\frac{\partial}{\partial y} \left[ \frac{P}{\rho} + \frac{\overline{v^2}}{2} \right] = \frac{U^2 + \overline{u^2}}{R(1 + y/R)}, \quad (6)$$

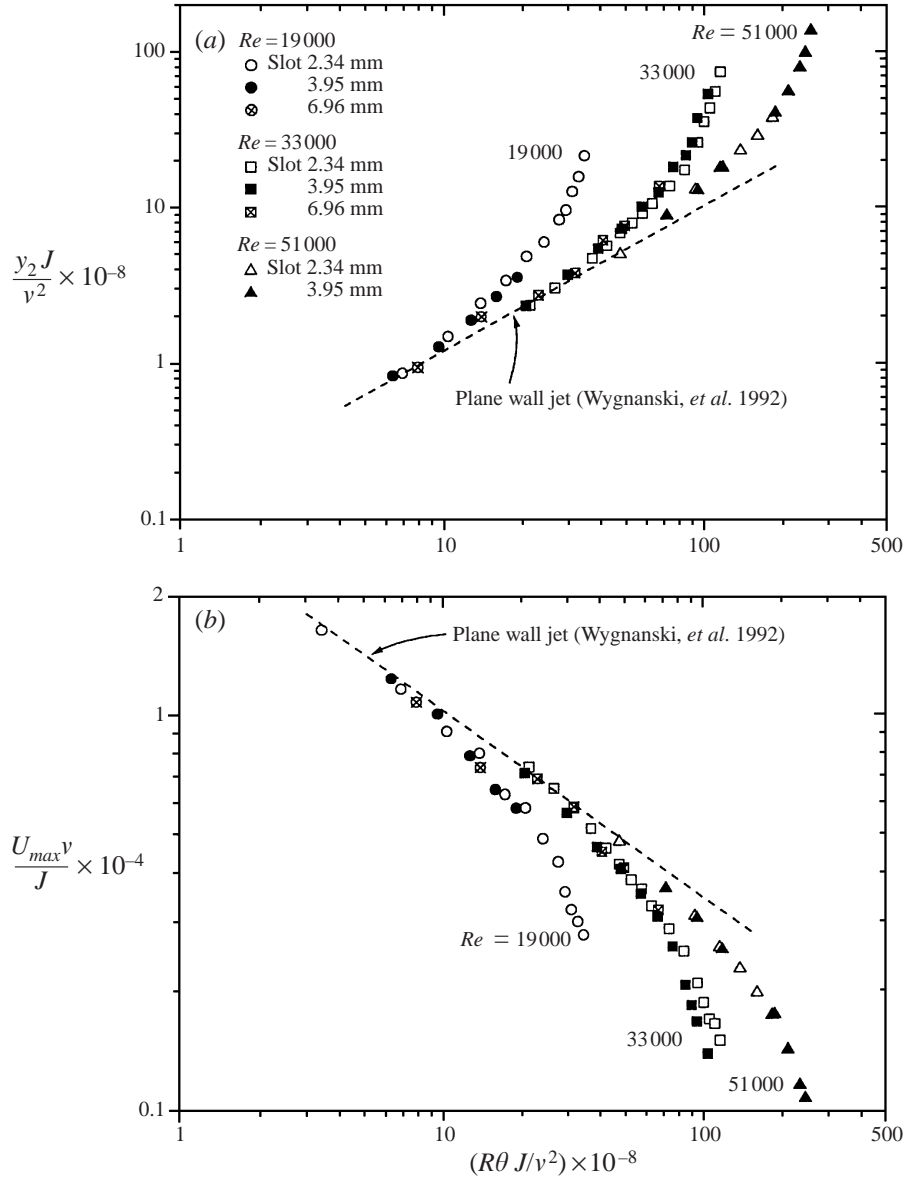


FIGURE 10. (a) The decay of the maximum velocity and (b) the radial rate of spread in the direction of streaming. Scaling based on the kinematic momentum flux  $J$  and the fluid viscosity  $\nu$ .

which upon integration and normalization gives

$$c_p = \frac{(P_\infty - P_s)R}{\frac{1}{2}\rho J_N} = \frac{2}{J_N} \int_0^\infty \frac{(U^2 + \overline{u'^2}) dy}{1 + y/R}. \quad (7)$$

This normalization was chosen since to first-order of approximation  $J_N = (2b/\rho)(P_0 - P_\infty)$  and  $P_0$  is the total pressure in the settling chamber. The integral on the right-hand side of the equation represents  $J$  and thus, under ideal conditions (when  $J_N = J$ ),  $c_p = 2$ . One may quickly assess the value of  $c_p$  in the fully developed, self-similar region ( $40^\circ \leq \theta \leq 120^\circ$ ) by assuming the jet to be thin (i.e.  $y/R \rightarrow 0$ ) and

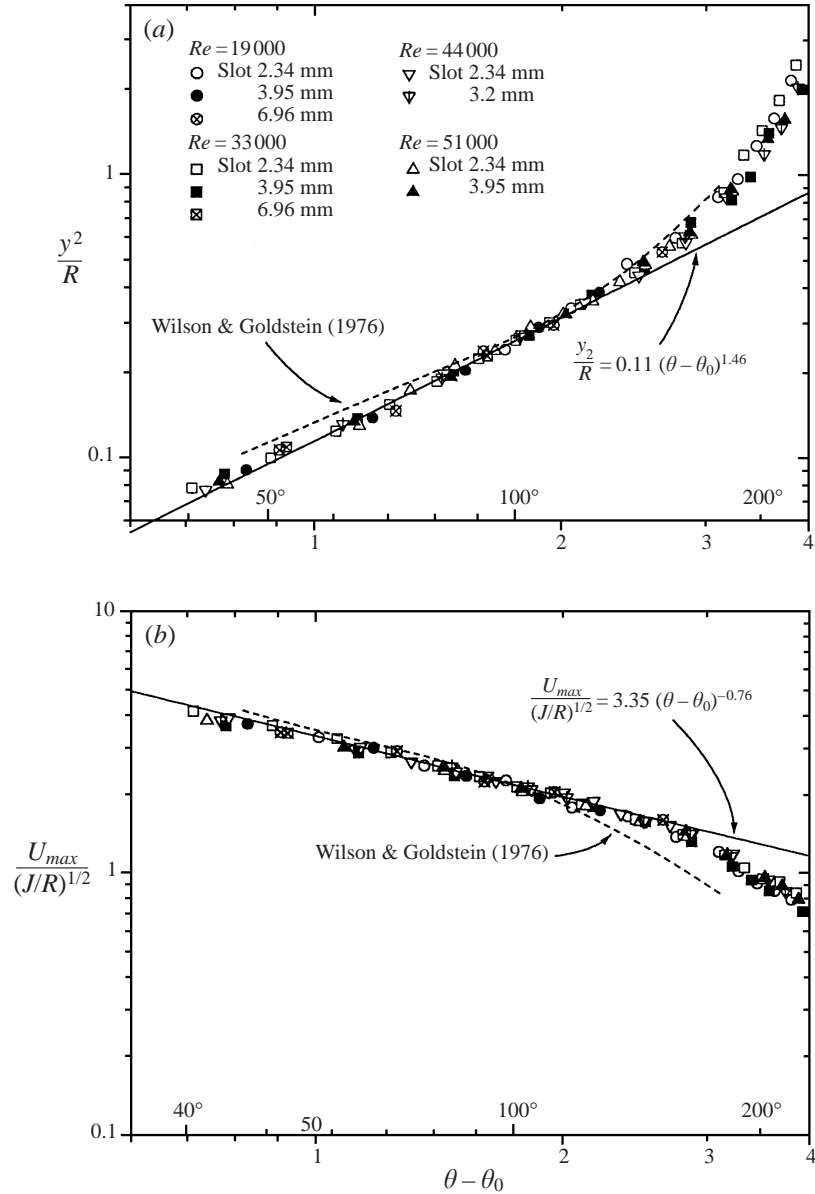
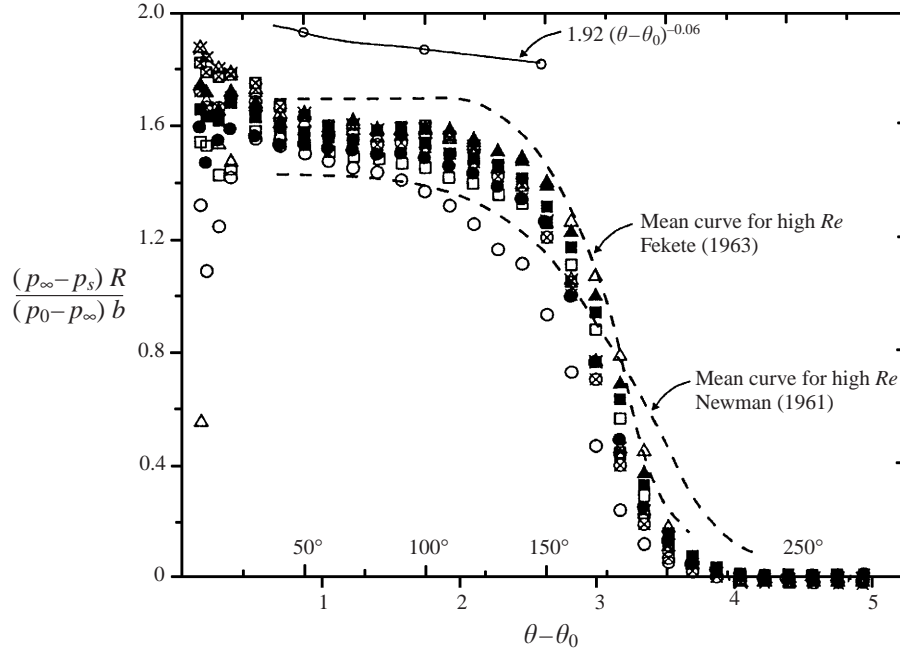


FIGURE 11. (a) The decay of the maximum velocity and (b) the radial rate of spread in the direction of streaming. Scaling based on the kinematic momentum flux  $J$  and the cylinder radius  $R$ .

neglecting the contribution of the turbulence intensity to the total momentum flux. In this case,  $c_p = 1.56 U_{max}^2 y_2 = 1.92(\theta - \theta_0)^{-0.06}$ , when the appropriate scaling values are substituted from equation (3). The complete right-hand side of equation (7) is plotted in figure 12. The agreement between this calculation and the measured  $c_p$  is reasonable up to  $\theta = 160^\circ$ . At larger azimuthal angles, the validity of the boundary-layer approximation becomes questionable and higher-order terms have to be included.


 FIGURE 12. Surface pressure coefficient  $c_p$  for various  $Re_N$ .

Newman (1961) derived the scaling parameters for the surface pressure by using dimensional analysis, assuming the flow to be incompressible and governed by

$$(P_0 - P_s), b, R, \rho, \nu,$$

where  $\nu$  is the kinematic viscosity of the fluid.

Thus, the surface pressure coefficient  $c_p$ , at an angular position  $\theta$ , is a function of these parameters. Newman realized that at some distance from the nozzle the flow will be independent of the separate parameters  $(P_0 - P_s)$  and  $b$ , but will depend on their product instead [i.e.  $(P_0 - P_\infty)b = 2\rho J_N$ ] leading to

$$c_p = \frac{(P_\infty - P_s) R}{P_0 - P_\infty) b} = f \left[ \theta, \left( \frac{(P_0 - P_\infty) R b}{\rho \nu^2} \right)^{1/2} \right], \quad (8)$$

where Newman's Reynolds number  $Re_N = ((P_0 - P_\infty) R b / \rho \nu^2)^{1/2}$  contains the product of the two lengthscales. The same quantity appeared in conjunction with the scaling of the mean velocity distribution in this flow (see equation (2)). For large values of this Reynolds number,  $c_p$  should also become independent of  $Re_N$  as it did in the case of the mean velocity. Thus, the surface pressure becomes merely a function of  $\theta$ . It remains to be seen whether the independent ratio  $b/R$ , which was thus far neglected, is of any significance. In order to answer this question, the slot width  $b$  and the initial jet velocity  $U_{jet}$  were varied in a manner that maintained constant Reynolds numbers ( $Re_N$  19 000,  $Re_N$  33 000 and  $Re_N$  51 000) for different ratios  $b/R$ . The symbols representing the nine independent experiments are given in table 1. The surface pressure distributions along the cylinder for tabulated inflow conditions are plotted in figure 12 and compared with former experiments by Fekete and Newman. The results of Fekete are surprising since they were obtained on the same cylinder 30 years earlier.

---

Slot width (mm)	$b/R$	$Re_N 19\,000$	$Re_N 33\,000$	$Re_N 51\,000$
2.34	0.023	○	□	△
3.95	0.039	●	■	▲
6.95	0.068	⊗	⊗	⊗

---

TABLE 1. Symbols representing the nine independent experiments

There is a consistent difference of approximately  $0.04 c_{p,max}$  between the present results and those of Fekete (Newman 1969), Newman's (1961) results are different; however, the differences between the present data and Newman's is attributed to the different settling chamber geometries. An exterior settling chamber, used in Newman's earlier experiment might have generated an adverse pressure, reducing  $c_p$  and its dependence on  $\theta$ . Our observed pressure coefficient is very nearly constant between  $\theta = 40^\circ$  and  $\theta = 120^\circ$  and then decreases rapidly to the surrounding pressure. At  $\theta \approx 220^\circ$  the pressure on the surface is atmospheric and the flow breaks away from the surface.

The surface pressure coefficient in the constant pressure region ( $40^\circ \leq \theta \leq 120^\circ$ ) becomes independent of  $Re_j = U_{jet} b/\nu$  for  $Re_j > 5 \times 10^3$ . This is consistent with other observations made on the dependence of the plane wall jet on  $Re_j$  (Wygnanski *et al.* 1992). Since the pressure coefficient near the slot is very sensitive to entrainment, it is also sensitive to  $Re_j$  and to the detailed geometry of the nozzle in relation to the circular cylinder. Both variables determine the transition location in the initial mixing layer formed between the constant velocity stream and the ambient fluid, and affect the initial value of  $c_p$ . Enormous pressure oscillations as well as fairly low, absolute values of the mean  $c_p$  were observed near thin slots (see data corresponding to  $b/R = 0.023$  in figure 12). Large slot widths generated larger initial values of  $c_p$  which were maintained throughout the constant pressure region. Since the rate of entrainment of the mixing layer is higher than in the fully developed wall jet, a larger slot generates a larger absolute value of  $c_p$  at a constant  $Re_N$ , provided that  $Re_j > 5000$ . Nakaguchi (1961) attributed the high pressure coefficient which he observed near the slot to the existence of a separation bubble; however, no separation bubbles were detected in the present study. Surface visualization was used initially; more recently, however, the fluid emerging from the slot was seeded with smoke particles and a two dimensional laser sheet illumination was used. No bubble was observed near the slot. The scatter apparent in figure 12 can be reduced by recalling that  $J_N$  is only an approximation to the jet momentum, because the flow expands from the settling chamber to the local static pressure prevailing near the nozzle,  $P_s$ . Thus, if  $J = (2b/\rho)(P_0 - P_s)$ , then the modified pressure coefficient

$$[c_p]_M = \frac{(P_\infty - P_s)R}{\frac{1}{2}\rho J} = \frac{(P_\infty - P_s)R}{J_N(1 + c_p b/R)} = \frac{c_p}{(1 + c_p b/R)} \quad (9)$$

reduces the scatter but does not eliminate it entirely.

## 6. Skin friction and mean momentum balance

The skin friction coefficient was determined from the slope of the mean velocity profile close to the surface. This measuring technique was adopted earlier for the

plane wall jet. It is based on 6–10 data points taken in the region where the velocity gradient is linear. In the present case, it allowed a re-examination of the character of the velocity distribution prior to separation. Specifically, it was searched for the occurrence of inflection points in the adverse pressure gradient region seen prior to the mean separation location. When the skin friction is normalized by the local maximum velocity  $\tau_w/\rho U_{max}^2$  it appears to increase with increasing  $\theta$  attaining a maximum value around  $\theta = 140^\circ$  (figure 13*b*). This behaviour stems from changes in  $U_{max}$  rather than in  $\tau_w$ . Using  $J_N/R$  for normalization indicates that  $c_f$  decreases monotonically with increasing distance from the nozzle (figure 13*c*). The centrifugal forces associated with the convex curvature reduce  $c_f$ . The  $c_f$  measured here is one-third of the corresponding  $c_f$  measured in the plane wall jet configuration (figure 13*d*).

The consistency of the measurements, the validity of the boundary-layer approximation and the two-dimensionality of the flow may now be assessed by constructing a control volume around the cylinder and checking the mean momentum balance. Starting at  $\theta = 40^\circ$ , where similarity of the mean flow was observed, and considering the constant pressure region first (i.e. going around a quarter of the circle up to  $\theta = 130^\circ$ ) yields the following balance in the vertical direction (see figure 14):

$$\left[ \int_0^\infty \{ (c_p J/2R) - U^2 \} dy \right]_{\theta=130^\circ} + \frac{1}{2} J \int_0^{\pi/2} \left( c_p \cos \theta + \frac{R}{b} c_f \sin \theta \right) d\theta = 0, \quad (10)$$

the sum of all four terms computed from the data amounts to  $(0.036 J)$  proving the overall consistency of the measurements and the two-dimensionality of the flow. The contribution of the skin friction to this balance is minimal  $0.015 J$  and therefore this momentum budget cannot be used as a proof of reliability of this data. This exercise may be repeated between  $\theta = 40^\circ$  and  $220^\circ$  by assuming that the jet enters and leaves the control volume in the horizontal direction giving

$$\frac{1}{2} J \int_0^\pi \left( C_p \cos \theta + \frac{R}{b} C_f \sin \theta \right) d\theta = 0. \quad (11)$$

This assumption is faulty because the vertical component of the friction force is much smaller than the pressure force, giving an imbalance of approximately  $0.54 J$ . A momentum budget in the horizontal direction yields a comparable imbalance of  $0.65 J$  suggesting that at  $\theta = 220^\circ$  the mean momentum of the jet is inclined to the surface of the cylinder at approximately  $\theta = 40^\circ$ . This is confirmed by flow visualization (figure 15). The data is self consistent but it does not explain the mechanism responsible for the sudden broadening of the inner flow (figure 7*c*) leading to its separation from the surface.

Streamlines calculated by assuming that the flow is two-dimensional are plotted in figure 16*(a)*. The onset of strong divergence appears around  $\theta = 180^\circ$  implying a rapid deceleration in the direction of streaming and an increase in the normal component of velocity invalidating the boundary-layer approximation. The integrated component of the jet momentum in the direction normal to the surface is also plotted in figure 16*(b)*. It indicates a rapid increase in the  $y$ -component of momentum at  $\theta > 180^\circ$ . This corroborates the findings of the control volume analysis and coincides with the region in which the value of the shape factor  $H$  increased rapidly (figure 8). The earliest indicator for the failure of the boundary-layer approximation is the width of the flow. Although  $y_2$  represents approximately half of the jet width, it becomes comparable to  $R$  long before the onset of the rapid flow divergence. In fact  $y_2 = R$

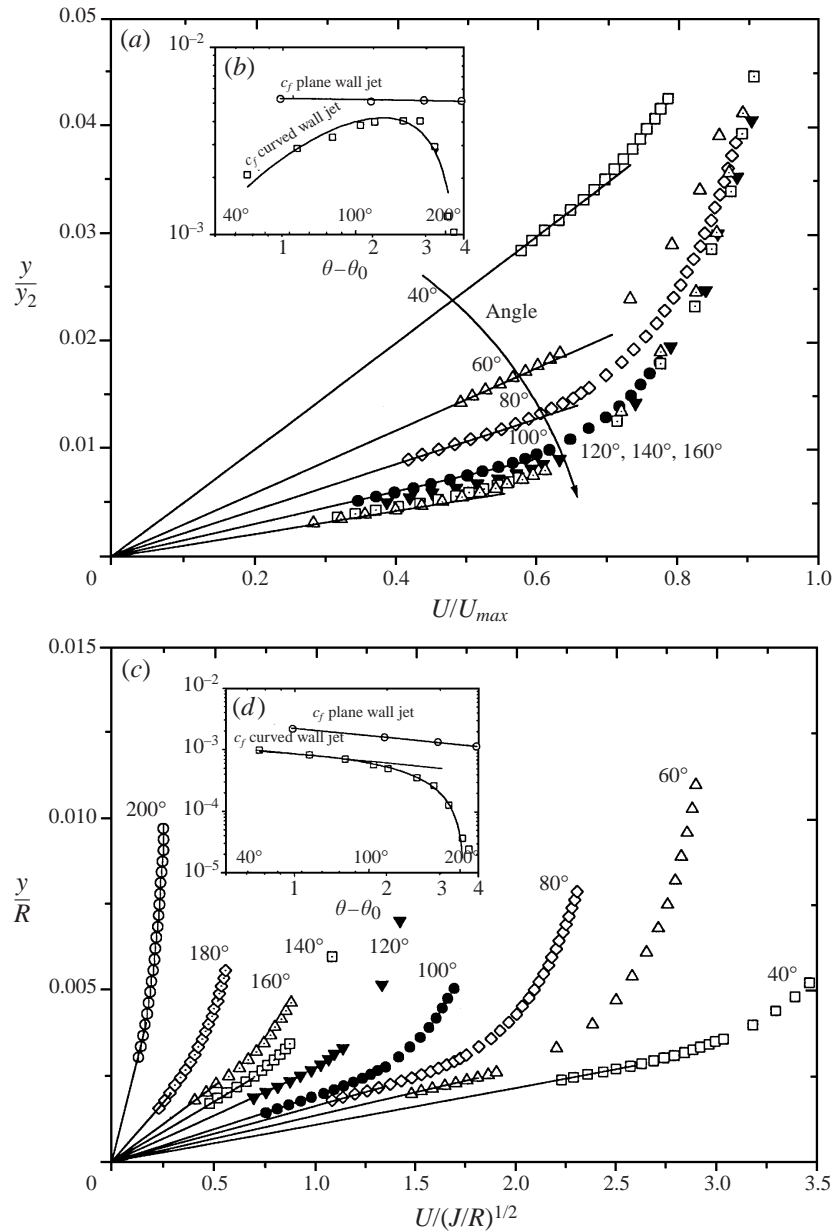


FIGURE 13. (a), (c) Streamwise component of velocity in the immediate vicinity of the surface. (b), (d) A comparison of the skin friction coefficient  $c_f$  in the curved and in the plane wall jet.

around  $\theta = 180^\circ$  (figure 16a). Near the nozzle ( $\theta < 40^\circ$ ), the entrainment is so strong as to generate an appreciable negative  $J_{normal}$ .

## 7. Turbulent intensities and Reynolds stress

The streamwise component of the turbulence intensity is plotted in figure 17(a) for five, equally spaced, values of  $\theta$  ranging from  $\theta = 40^\circ$  to  $200^\circ$ . Data ob-



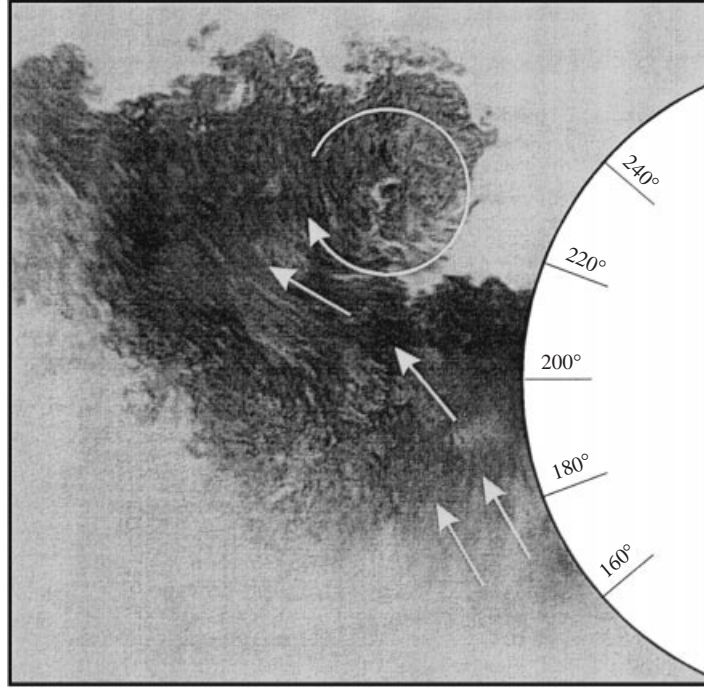


FIGURE 15. Flow visualization in the separation region.

that  $y_2$  increases rapidly with  $\theta$  when  $\theta \geq 180^\circ$ . There is a correlation between the production of turbulent energy near the surface ( $\overline{u'v'}(\partial U/\partial y)$ ) and the maximum intensity of  $u'$  observed. Some of it is masked by normalizing the turbulence by local  $U_{max}$  (see also figures 13(c) and 13(d)); however, plotting  $(\overline{u^2}/J/R)^{1/2}$  does not alter the distribution of  $(\overline{u'})^{1/2}$  with  $y/y_2$ . The distribution of  $(\overline{u^2})^{1/2}/U_{max}$  with  $y/y_2$  is plotted on an expanded scale in figure 17(b). The radial component of the velocity fluctuations  $(\overline{v^2})^{1/2}/U_{max}$  is initially comparable with its counterpart on the flat plate, but its magnitude doubles over the range  $40^\circ \leq \theta \leq 200^\circ$  (figure 17c). The radial location at which the local value of  $(\overline{v^2})^{1/2}/U_{max}$  is maximum decreases with respect to  $y_2$  with increasing  $\theta$ . Therefore, at  $\theta = 40^\circ$   $y_{(v'=max)}/y_2 = 0.7$  while at  $\theta = 200^\circ$   $y_{(v'=max)}/y_2 = 0.35$ . It might be expected that the  $y$ -location at which  $u'v'$  attains its maximum will also decrease relative to  $y_2$ , at large values of  $\theta$ ; however, this was not the case, as may be noted in figure 17(e). Between  $\theta = 40^\circ$  and  $\theta = 200^\circ$ :  $[(\overline{u^2})^{1/2}/U_{max}]_{max}$  increased by a factor of 1.65,  $[(\overline{v^2})^{1/2}/U_{max}]_{max}$  increased by a factor of 2 and  $|\overline{u'v'}/U_{max}^2|_{max}$  by a factor of 2.4; however,  $U_{max}$  decreased by a factor of 4 in this  $\Delta\theta$  interval. The ratio between  $(u'/v')_{max}$  decreased from 1.4 at  $\theta = 40^\circ$ , to 1.08 at  $\theta = 160^\circ$ . The maximum of the  $\overline{u'v'}$  correlation (figure 18) exceeds 0.53 which is larger than in the plane wall jet (where  $\overline{u'v'}/(\overline{u^2})^{1/2}(\overline{v^2})^{1/2} = 0.49$ ) and significantly larger than in the turbulent boundary layer over a flat plate. The radial location at which  $\overline{u'v'}/(\overline{u^2})^{1/2}(\overline{v^2})^{1/2}$  attains its maximum value increases with  $\theta$  from being at  $y/y_2 = 0.5$  at  $\theta = 40^\circ$  to  $y/y_2 = 1$  at  $\theta = 160^\circ$ . Since these observations are peculiar to this flow they suggest that surface curvature, and the centrifugal force generated by it, alter the turbulent structure.

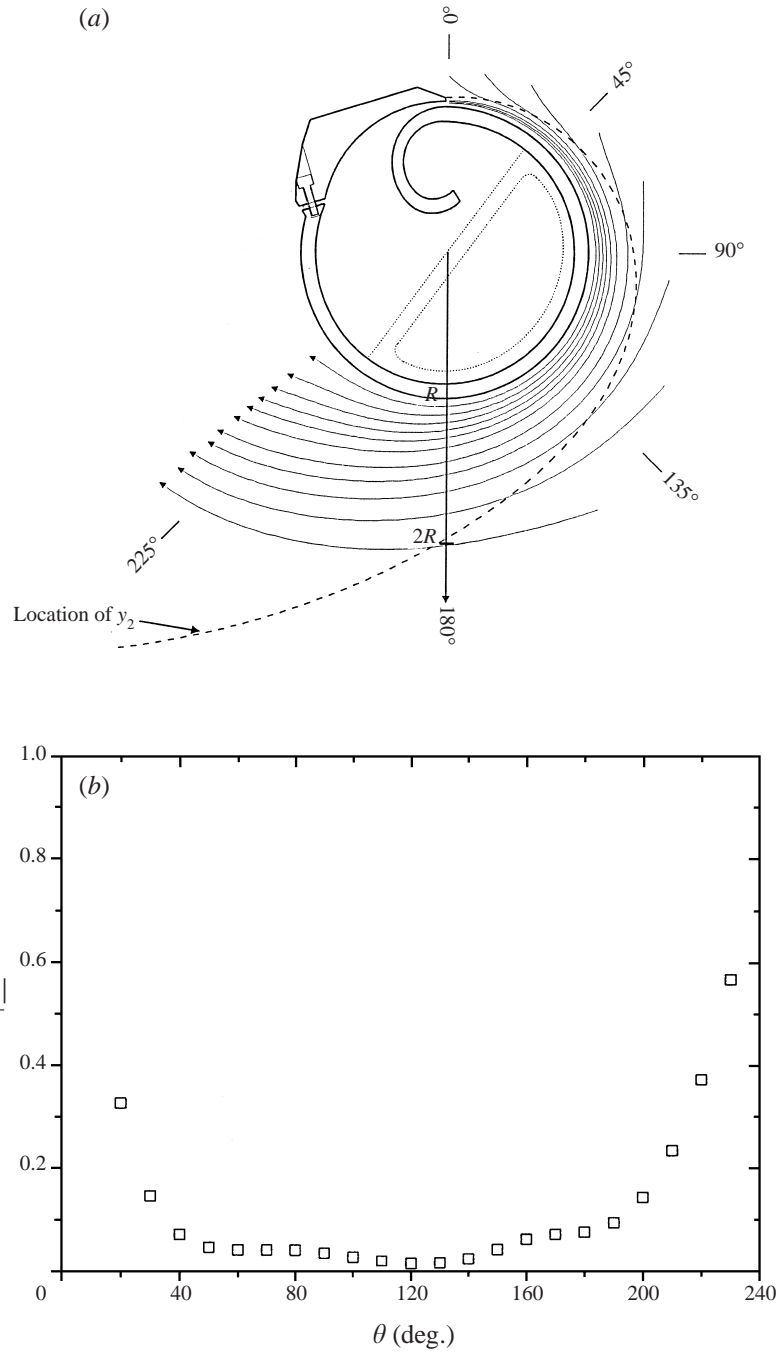


FIGURE 16. (a) Streamline calculation and (b) radial momentum  $J_{normal}$ .

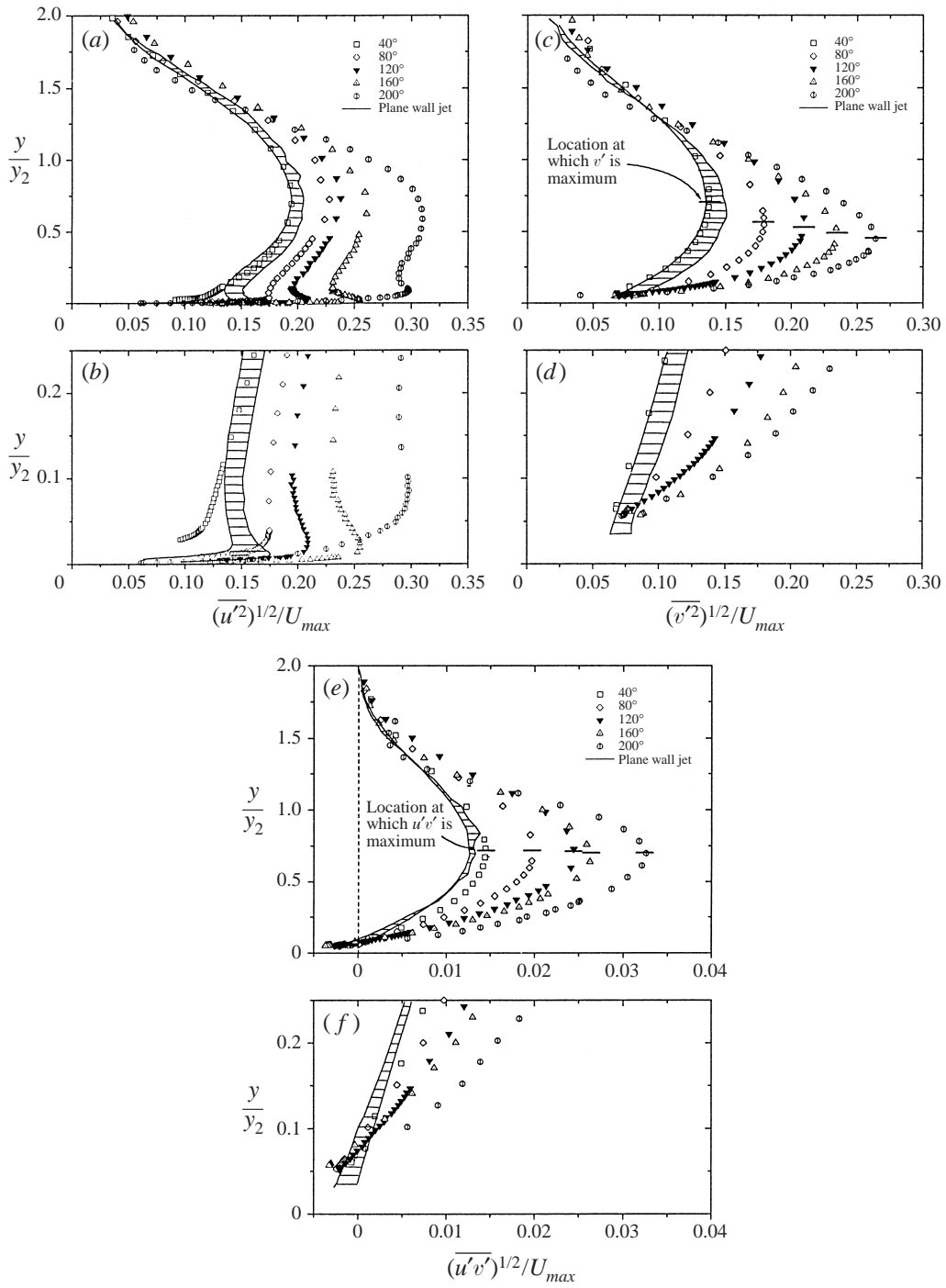


FIGURE 17. A comparison of turbulence intensities and Reynolds stresses in the plane and curved wall jet.

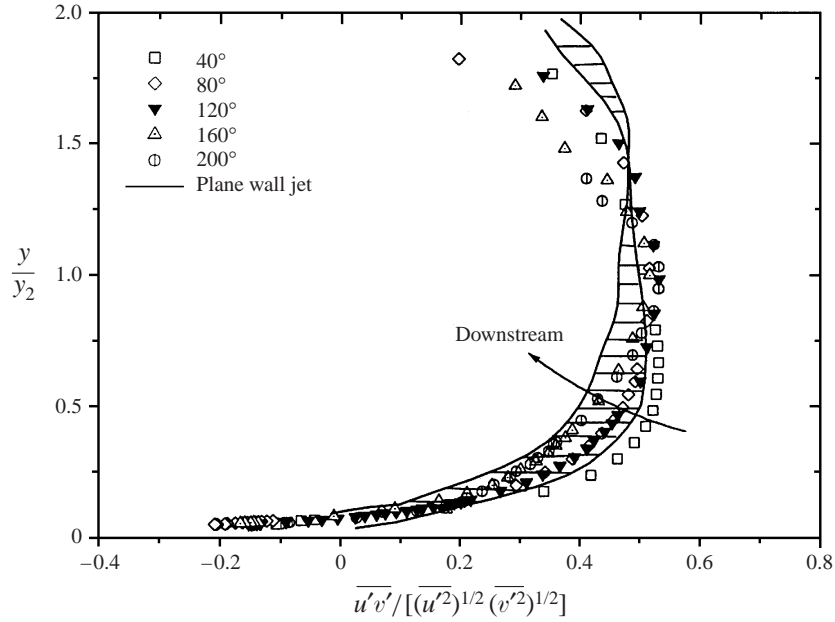


FIGURE 18. The Reynolds stress correlation.

The Reynolds stress was calculated from the momentum equation in the direction of streaming (equation (12)) which included the pressure gradient term obtained from the normal momentum equation (equation (13)) but neglected the viscous term:

$$\begin{aligned}
 U \frac{\partial U}{\partial s} + \left(1 + \frac{r}{R}\right) V \frac{\partial U}{\partial r} + \frac{UV}{R} &\equiv \frac{\partial U^2}{\partial s} + \left(1 + \frac{r}{R}\right) \frac{\partial UV}{\partial r} + 2 \frac{UV}{R} \\
 &= -\frac{1}{\rho} \frac{\partial p}{\partial s} - \frac{\partial \overline{u^2}}{\partial s} - \left(1 + \frac{r}{R}\right) \frac{\partial \overline{u'v'}}{\partial r} - 2 \frac{\overline{u'v'}}{R}, \quad (12)
 \end{aligned}$$

$$\begin{aligned}
 U \frac{\partial V}{\partial s} + \left(1 + \frac{r}{R}\right) V \frac{\partial V}{\partial r} - \frac{U^2}{R} &\equiv \frac{\partial UV}{\partial s} + \left(1 + \frac{r}{R}\right) \frac{\partial V^2}{\partial r} + \frac{V^2 - U^2}{R} \\
 &= -\left(1 + \frac{r}{R}\right) \frac{1}{\rho} \frac{\partial p}{\partial r} - \frac{\partial \overline{u'v'}}{\partial s} - \left(1 + \frac{r}{R}\right) \frac{\partial \overline{v^2}}{\partial r} - \frac{\overline{v^2} - \overline{u^2}}{R}. \quad (13)
 \end{aligned}$$

Although the inertia terms contributed the largest share to the calculated  $\overline{u'v'}$ , the contribution of the pressure gradient was not negligible even when the surface pressure indicates that  $(\partial p / \partial x) \Rightarrow 0$ . Neglecting the pressure gradient term in these calculations would overestimate the maximum value of  $\overline{u'v'}$  by more than 10% in the range of  $\theta$  considered. The calculated pressure coefficients within the flow are not shown because they could not be compared with any measurements. The viscous terms, on the other hand, are truly negligible except in the immediate vicinity of the surface. The results agree well with the measurements up to and including  $\theta = 120^\circ$  (figure 19a). They indicate that the mean flow is two-dimensional up to this  $\theta$  and that the measurements of velocity are fairly accurate. The agreement between measured and calculated  $\overline{u'v'}$  is not only a proof of data consistency but it also validates the boundary-layer approximation within this region. Another measure of the two-dimensionality of the flow is the ratio between

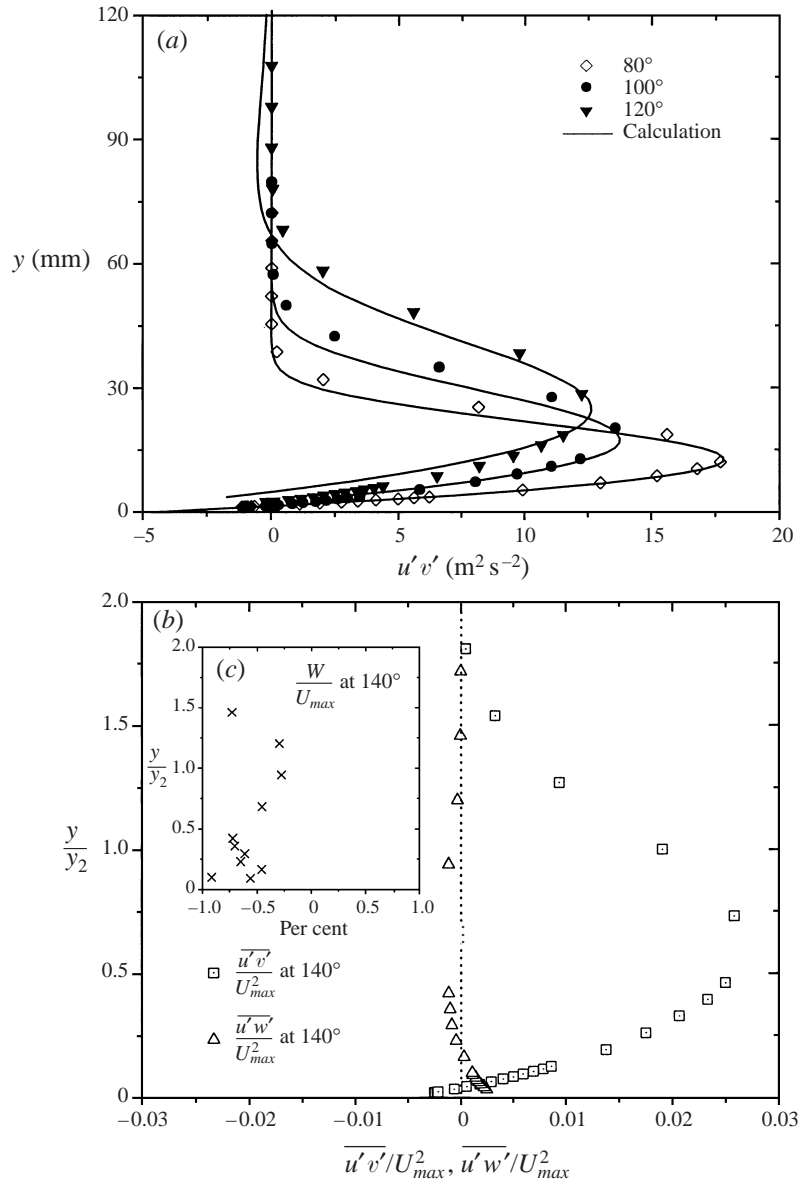


FIGURE 19. A comparison of measured and calculated Reynolds stresses.

the measured  $\overline{u'w'}$  and  $\overline{u'v'}$ . Both quantities are plotted in figure 19(b) for measurements made at  $\theta = 140^\circ$ . Even the mean spanwise velocity  $W$  was measured at that  $\theta$  (figure 19c) and was found to be negligible.

## 8. Conclusions

It is well known that adherence of jets to nearby surfaces is caused by entrainment. It appears that the separation of jets from curved surfaces can also be attributed to entrainment which destroys the sensitive balance between the centrifugal and the pressure forces normal to the mean flow direction. The process of separation is

complex, the centrifugal instability generates large eddies and enhances the turbulence level well beyond the norm in comparable plane wall jets. The large eddies, which are most effective in entraining external fluid, result in a rapid broadening of the jet, its deceleration and the generation of a mean velocity component normal to the surface. When the normal velocity component becomes comparable to the tangential one, the flow separates. The present measurements indicate that the boundary-layer approximation, used to describe turbulent jets of all kinds, fails (a long time) before the onset of separation. This suggests that entrainment acts like a double-edged sword, a threshold value is required for a jet to adhere to a surface, but it should be kept to a minimum in order to prevent or delay its separation from the surface.

The project was sponsored in part by AFOSR under grant F4962-096-10187. The apparatus was loaned to us by Professors B. G. Newman and G. I. Fekete from McGill University. One of us (R. N.) started on this project owing to a cooperation agreement between the University of Arizona and the Technical University Berlin.

## REFERENCES

- BRADSHAW, P. 1969 Effects of streamline curvature on turbulent flow. *AGARDograph* 169.
- FEKETE, G. I. 1963 Coanda flow of a two-dimensional wall jet on the outside of a cylinder. *Rep.* 63-11. McGill University, Department of Mechanical Engineering.
- FUJISAWA, N. & KOBAYASHI, R. 1987 Turbulence characteristics of wall jets along strong convex surfaces. *J. Mech. Sci.* **29**, 311–320.
- GUITTON, D. E. 1964 Two-dimensional turbulent wall jets over curved surfaces. *Rep.* 64-7. McGill University, Department of Mechanical Engineering.
- LAUNDER, B. E. & RODI, W. 1981 The turbulent wall jet. *Prog. Aerospace Sci.* **19**, 81–128.
- NAKAGUCHI, H. 1961 Jet along a curved wall. *Res. Memo.* 4. Department of Aeronautics, University of Tokyo.
- NARASIMHA, R., NARAYAN, K. Y. & PARTHASARATHY, S. P. 1973 Parametric analysis of turbulent wall jets in still air. *Aerospace J.* **77**, 335.
- NEWMAN, B. G. 1961 The deflection of plane jets by adjacent boundaries—Coanda effect. In *Boundary Layer and Flow Control* (ed. G. V. Lachman), pp. 232–251. Pergamon.
- NEWMAN, B. G. 1969 The prediction of turbulent jets and wall jet. *Can. Aeronaut. Space J.* **15**, 287–304.
- RAYLEIGH, LORD 1916 On the dynamics of revolving fluids. *Proc. R. Soc. Lond.* **93**, 148.
- TOWNSEND, A. A. 1956 The properties of equilibrium boundary layers. *J. Fluid Mech.* **1**, 561–573.
- TOWNSEND, A. A. 1962 The behaviour of a turbulent boundary layer near separation. *J. Fluid Mech.* **12**, 536–554.
- WILSON, D. J. & GOLDSTEIN, R. J. 1976 Turbulent wall jet with cylindrical streamwise surface curvature. *Trans. ASME I: J. Fluids Engng* **98**, 550–557.
- WYGNANSKI, I., KATZ, Y. & HOREV, E. 1992 On the applicability of various scaling laws to the turbulent wall jet. *J. Fluid Mech.* **234**, 669–690.
- YOUNG, T. 1800 Outlines of experiments and inquiries respecting sound and light. Lecture to the Royal Society. *J. R. Aero. Soc.* **61**, 157.
- ZHOU, M. D., ROTHSTEIN, J. & WYGNANSKI, I. 1992 On the hydrodynamic stability of the wall jet. *11th Austral. Fluid Mech. Conf.*
- ZHOU, M. D., HEINE, CHR. & WYGNANSKI, I. 1996 The effect of excitation on the coherent and random motion in plane wall jet. *J. Fluid Mech.* **310**, 1–37.